

# SCUBA Observations of NGC 1275

Judith A. Irwin,<sup>1</sup> J. M. Stil,<sup>1</sup> and T. J. Bridges<sup>2</sup>

<sup>1</sup>*Dept. of Physics, Queen's University, Kingston, Canada, K7L 3N6*

<sup>2</sup>*Anglo-Australian Observatory, PO Box 296, Epping, NSW 2121, Australia*

Accepted xxx. Received xxx;

## ABSTRACT

Deep SCUBA observations of NGC 1275 at  $450\mu\text{m}$  and  $850\mu\text{m}$  along with the application of deconvolution algorithms have permitted us to separate the strong core emission in this galaxy from the fainter extended emission around it. The core has a steep spectral index and is likely due primarily to the AGN. The faint emission has a positive spectral index and is clearly due to extended dust in a patchy distribution out to a radius of  $\sim 20$  kpc from the nucleus. These observations have now revealed that a large quantity of dust,  $\sim 6 \times 10^7 M_{\odot}$ , 2 orders of magnitude larger than that inferred from previous optical absorption measurements, exists in this galaxy. We estimate the temperature of this dust to be  $\sim 20$  K (using an emissivity index of  $\beta = 1.3$ ) and the gas/dust ratio to be 360. These values are typical of spiral galaxies. The dust emission correlates spatially with the hot X-ray emitting gas which may be due to collisional heating of broadly distributed dust by electrons. Since the destruction timescale is short, the dust cannot be replenished by stellar mass loss and must be externally supplied, either via the infalling galaxy or the cooling flow itself.

## Key words:

methods: data analysis – ISM: dust – galaxies: individual: NGC 1275 – galaxies: cooling flows – galaxies: clusters: individual: Perseus.

## 1 INTRODUCTION

Until recently, it was not thought that centrally-located cluster galaxies contained significant amounts of dust. However, recent observations have begun to reveal large amounts of dust in some central galaxies. The existence of dust is inferred from a diverse set of observations, including the ratios of emission lines in optical filaments (Hu 1992; Donahue & Voit 1993; Crawford et al. 1999), dust lanes in optical images (e.g. McNamara, O'Connell & Sarazin 1996; Pinkney et al. 1996), near infrared (NIR) imaging and spectroscopy (e.g. Krabbe et al. 2000; Donahue et al. 2000; Jaffe, Bremer, & van der Werf 2000), and X-ray absorption (e.g. White et al. 1991; Allen & Fabian 1997; Arnaud & Mushotzsky 1998; Allen 2000).

Searches at longer wavelengths have now also revealed emission from dust directly, especially cooler dust which may be much more plentiful than the warmer components. The Infrared Astronomical Satellite (IRAS) detected several central cluster galaxies at  $60$  and  $100 \mu\text{m}$ ; Cox, Bregman, & Schombert (1995) find that  $\sim 10\%$  of central galaxies have far infrared (FIR) emission, with dust masses of  $\sim 10^7 M_{\odot}$ . More recently, Lester et al. (1995) have detected  $100 \mu\text{m}$  emission from NGC 1275 with the Kuiper Airborne Observatory (KAO), and there have been Infrared Space Observa-

tory (ISO) detections at  $60$ – $200 \mu\text{m}$  of a few central galaxies (e.g. Hansen et al. 2000). Annis & Jewitt (1993) carried out an unsuccessful search for dust emission in 11 cooling flow clusters using the UKT-14 bolometer system on the James Clerk Maxwell Telescope (JCMT). More recently, however, Edge et al. (1999) have detected dust emission at  $850 \mu\text{m}$  in two cooling flow clusters using the more sensitive Submillimetre Common-User Bolometer Array (SCUBA) camera.

The origin of the dust in central cluster galaxies is a matter of some controversy. Central cluster galaxies live in complicated environments, with many at the centers of cluster cooling flows (e.g. Fabian 1994), and interactions/mergers may also be common. Dust in central cluster galaxies may thus originate in several ways: from the cooling flow itself or in cold, dense clouds condensed from the flow; from ongoing star formation, perhaps initiated by the cooling flow; or from the merger of a gas/dust rich galaxy. Direct detections of dust in central cluster galaxies, and good determinations of the dust properties (mass, temperature, and correlations with other components) will help enormously to decide between these alternatives. For example, the bulk of the dust in cooled gas clouds is expected to be quite cold with  $T < 15\text{K}$  (e.g. Fabian, Johnstone, & Daines 1994; Johnstone, Fabian & Taylor 1998) [However, this conclusion is disputed by O'Dea, Baum & Gallimore (1994) and Voit &

arXiv:astro-ph/0107030v1 2 Jul 2001

Donahue (1995), who claim minimum dust temperatures of  $\sim 20$  K.]

The very existence of dust in central cluster galaxies is in itself surprising, since any dust should be destroyed quickly by sputtering from X-rays from the hot cluster gas, on timescales  $\leq 10^7$  years (e.g. Draine & Salpeter 1979). Either the dust is shielded against sputtering (e.g. at the centers of cold, dense molecular clouds), or the dust is replenished on similar timescales. This issue is discussed in more detail in Sect. 4.2.

NGC 1275 is a complex and fascinating object. It has been studied in virtually every waveband, including the optical (e.g. Nørgaard-Nielsen et al. 1993; McNamara et al. 1996), NIR (e.g. Donahue et al. 2000; Krabbe et al. 2000) and far infrared (FIR) (Gear et al. 1985; Lester et al. 1995). It has been classified as a Seyfert (Seyfert 1943) and has an active galactic nucleus (AGN) in the form of the highly variable radio source 3C 84 (e.g. Pedlar et al. 1990). Minkowski (1957) discovered two distinct filamentary systems around NGC 1275. The low velocity system (LVS) has the same velocity ( $\sim 5300$  km s $^{-1}$ ) as that of NGC 1275 itself, and has been studied in detail by several authors (e.g. Lynds 1970; Hu et al. 1983; Caulet et al. 1992). The high velocity system (HVS) has a velocity  $\sim 3000$  km s $^{-1}$  higher than NGC 1275 and consists of giant HII regions to the North and North-West of the galaxy center; it has generally been concluded that the HVS is a late-type spiral galaxy. At least part of the HVS is in front of the nucleus, as determined from HI absorption against the nuclear radio source (De Young, Roberts, & Saslaw 1973) and Ly $\alpha$  absorption (Briggs, Snijders, & Bokserberg 1982). The HVS could be merely a chance projection onto NGC 1275, but several authors have argued that the HVS is in fact colliding with NGC 1275 (e.g. Hu et al. 1983; Unger et al. 1990; Caulet et al. 1992; Nørgaard-Nielsen et al. 1993). Recent observations of gas at velocities intermediate between the LVS and HVS also strongly argue for a physical connection between the two systems (Ferruit et al. 1998).

It has been known for some time that the Perseus cluster hosts a large cooling flow (e.g. Fabian et al. 1981); analysis of recent Advanced Satellite for Cosmology and Astrophysics (ASCA) data show that the mass infall rate is  $\sim 300 M_{\odot}$  yr $^{-1}$  (Allen et al. 1999). Röntgen Satellite (ROSAT) and Chandra X-ray observations of NGC 1275 and the Perseus cluster (Böhringer et al. 1993, and Fabian et al. 2000, respectively) have also revealed two holes in the NGC 1275 X-ray emission, thought to be caused by displacement of hot gas by the radio lobes. NGC 1275 is the only cooling flow central galaxy with detected CO emission, with an inferred molecular H $_2$  mass of  $\sim 10^{10} M_{\odot}$ ; see Bridges & Irwin (1998) for a summary of the many previous CO studies.

In this paper, we present new SCUBA 450/850  $\mu$ m data for NGC 1275, in an attempt to study the cold dust in this galaxy in more detail. We are especially interested in such dust properties as: its spatial distribution and correlation with other components, total mass, temperature and ultimately, its origin. In Sect. 2, we present the observations and data reductions, unprocessed and processed images, Sect. 3 presents the results, including an analysis of the AGN and extended dust components, separately, and correlations with other wavebands, Sect. 4 discusses the origin of the dust and dust heating, and Sect. 5 presents the conclusions. For

NGC 1275, we take  $D = 70$  Mpc ( $H_0 = 75$  km s $^{-1}$  Mpc $^{-1}$ , Bridges & Irwin 1998).

## 2 OBSERVATIONS AND DATA REDUCTION

### 2.1 Maps of NGC 1275

Table 1 lists the observing log of SCUBA jiggle maps obtained on July 15, October 31 and December 14 1998. The total observation time was 5.5 hours, half of which was spent on the source. Chopping was performed in Azimuth, with a chop throw of 120 arcseconds.

The standard reduction scheme for SCUBA jiggle maps was followed, consisting of flatfielding, correction for atmospheric extinction, removal of noisy bolometers, sky noise removal and despiking. These steps are described in detail in Sandell (1997). Flatfielding corrects for differences in sensitivity of the bolometers. The atmospheric opacity at 450 and 850  $\mu$ m was determined from skydip observations. Noisy bolometers were identified from noise measurements performed in between observations, and visual inspection of the signal of all bolometers as a function of time during the observations.

Variations of the sky brightness are not canceled out completely by chopping because the atmosphere in the direction of the chopped beam is significantly different from the atmosphere in the direction of the source. This is a particular concern for observations of an extended source, where a large chop throw is required (Holland et al. 1999). Variations of the sky on short time scales were further eliminated by subtracting the median sky level measured by off-source bolometers for each 18 second integration. Although the sky level is determined with higher accuracy if more bolometers are considered, the likelihood that faint extended emission of the source is also subtracted, increases as well. A compromise must be sought between decreasing the sky noise and the possibility of subtracting source emission. The sky level was determined from the outer two rings of bolometers at 450  $\mu$ m, and the single outer ring of bolometers at 850  $\mu$ m. In this way a significant aperture around the centre of the field of view is excluded from the determination of the sky level. The radius of the aperture which is never covered by any of the ‘‘sky’’-bolometers is 28’’ at 450  $\mu$ m and 46’’ at 850  $\mu$ m. As the sky level at any time is taken to be the median of a ring of 54 (450  $\mu$ m) or 18 (850  $\mu$ m) bolometers surrounding the source, only a smooth symmetric component would be subtracted in this way.

Occasional spikes in the output of each bolometer were then removed by excluding signals deviating more than  $\pm 3\sigma$  from the mean signal.

The data were averaged with weight factors  $w_i = (t_i/N_i)^2$  where  $t_i$  and  $N_i$  are the integration time and noise level of observation  $i$ , to produce the maps shown in Fig. 1. These weight factors take into account both the different integration times and atmospheric opacities of the observations, since the noise in each map is dominated by the sky. The relative weights of the three nights are July:October:December=0.48:1:0.64.

Recently, a potential calibration problem resulting from erroneous values of the hot and cold load temperatures was identified (see

[http://www.jach.hawaii.edu/JACdocs/JCMT/SCD/SN/002/tau\\_analysis.html](http://www.jach.hawaii.edu/JACdocs/JCMT/SCD/SN/002/tau_analysis.html)). This problem could affect the sky opacity derived from skydip observations. The calibration was repeated with opacities calculated from the CSO opacity and the revised relations for the opacities at  $450\mu\text{m}$  and  $850\mu\text{m}$ . We found that this procedure had no effect on our calibration.

Taking into account the repeatability of the flux determination over a variety of integration times as well as an assessment of the accuracy of the calibration factor including uncertainties in the calibrator fluxes, we estimate that the  $450\mu\text{m}$  calibration error is  $\sim 25\%$  and the  $850\mu\text{m}$  error is  $\sim 10\%$ . Typical pointing corrections were 1 to 2 arcseconds over the course of an hour and residual pointing errors will be smaller than this.

The corrected, calibrated maps are shown in Fig. 1a ( $450\mu\text{m}$ ) and Fig. 1c ( $850\mu\text{m}$ ).

## 2.2 Beam maps

Beam maps were constructed for each night from calibrator maps with the same chop throw that was applied to the observations of NGC 1275. These calibrator maps were reduced in the same way as the observations of NGC 1275, with one exception: noisy bolometers were not excluded from the analysis. This was done to avoid the occurrence of unsampled areas in the planet maps. However no significant noise was introduced, because at  $850\mu\text{m}$  the primary calibrators Mars and Uranus are brighter than NGC 1275 by factors of 300 and 60 respectively. At  $450\mu\text{m}$  these factors are even larger because the brightness of the planets rises, whereas the spectrum of NGC 1275 shows a decline with frequency. Therefore, it is safe to conclude that noisy bolometers in the beam maps do not affect our results.

Calibrator sources are Uranus, Mars, CRL 618, and HL Tau. We used planet maps made with the same chop throw as the NGC 1275 maps, to define the shape of the beam for each night. Only for the  $450\mu\text{m}$  map in December, we used the secondary calibrator CRL 618, as no  $450\mu\text{m}$  planet map with the appropriate chop throw was available. The calibration factors adopted here are those determined for the October observations:  $623.69\text{ Jy}/(\text{Volt beam})$  at  $450\mu\text{m}$  and  $251.54\text{ Jy}/(\text{Volt beam})$  at  $850\mu\text{m}$ . Our largest calibrator was Mars which was smaller than  $5''$  over the course of the observations. This broadens the beam by less than  $0.3''$  at  $850\mu\text{m}$  and by less than  $0.6''$  at  $450\mu\text{m}$ , or  $< 1.8\%$  and  $< 6.7\%$  of the beam size, respectively (see caption to Figure 2 for the fitted beam size). Thus, the finite size of the calibrators will not significantly affect the beam, or its far sidelobes.

The coordinate system for the beam maps produced in this way was azimuth-elevation because chopping was done in azimuth, and the beam tends to be slightly elongated in the direction of chopping. For each observation of NGC 1275, the appropriate beam map was shifted to the position of the peak in the final map of NGC 1275, and rotated with the field rotation angle at the time of mid-observation. The resulting beam maps were coadded with the same weight factors as the data for NGC 1275 (see Sect. 2.1) to construct a map of the effective beam. The beam maps are shown in Fig. 1b and d. The most distinctive elongated feature in position angle  $\sim 40$  degrees visible in the  $850\mu\text{m}$  maps of

Num	Date	Time (Local)	Exp.time. (hour)	Airmass	$\tau_{850}$
130	Jul 15	05:25	0.5	1.276	0.23
131	Jul 15	05:53	0.5	1.202	0.23
134	Jul 15	06:29	0.5	1.135	0.26
135	Jul 15	06:58	0.5	1.102	0.26
144	Jul 15	08:08	0.5	1.079	0.29
145	Jul 15	08:36	0.5	1.091	0.29
148	Jul 15	09:12	0.5	1.128	0.30
12	Oct 31	02:11	1	1.160	0.16
57	Dec 14	00:23	1	1.326	0.18

**Table 1.** Observation log for SCUBA  $450/850\mu\text{m}$  observations of NGC 1275.

NGC 1275 and the final beam map, can be identified with the chop direction of the October 31 observation, which received a relatively high weight due to the favourable atmospheric conditions.

The resulting beam maps (Fig. 1b and d) give the best possible representation of the JCMT beam applicable to the coadded maps of NGC 1275. As only one calibrator observation with the correct chop throw was made in a night, we cannot correct for variations of the error lobes during the night. The main source of such variations is the sensitivity of the structure of the telescope to temperature variations. Large changes in the structure of the error lobes have been reported in the early evening (until 9pm) and in late morning (after 8am). However, only one observation, the  $850\mu\text{m}$  beam map of December 14, was made outside the relatively stable window between 9pm and 8am.

## 2.3 Processed Images

The beam shape begins to show irregular, non-gaussian patterns below the 5% level and it is desirable to remove such features from the total intensity image in order to see whether real residual emission remains. We attempted to do this by subtracting the scaled beam from the image; however, this assumes that the strong central source due to the AGN is strictly a point source and the result leaves some significant residual emission at the map center. We therefore treated the image like a typical radio map and applied deconvolution methods to remove the “dirty beam” and replace it with a “clean beam” with the same characteristics. The resulting maps retain the information from both the strong central source as well as any fainter extended emission, while removing the low level beam irregularities. Results using the CLEAN algorithm (Clark 1980), using the Astronomical Image Processing System (AIPS) routine, APCLN, are shown in Fig. 2a ( $450\mu\text{m}$ ) and Fig. 2d ( $850\mu\text{m}$ ) and results using the maximum entropy (ME) method (Cornwell & Evans 1985) using the AIPS routine, VTESS, are shown in Fig. 2b and Fig. 2e. A comparison of these maps provides an indication as to what emission is real. As the ME maps are well known to enhance faint, broad-scale structure but are less accurate than the clean maps in characterizing the emission quantitatively, we use the clean maps for all subsequent quantitative work.

Residual maps, i.e. after subtraction of all clean components, are shown in Fig. 2c and f. For these images, we

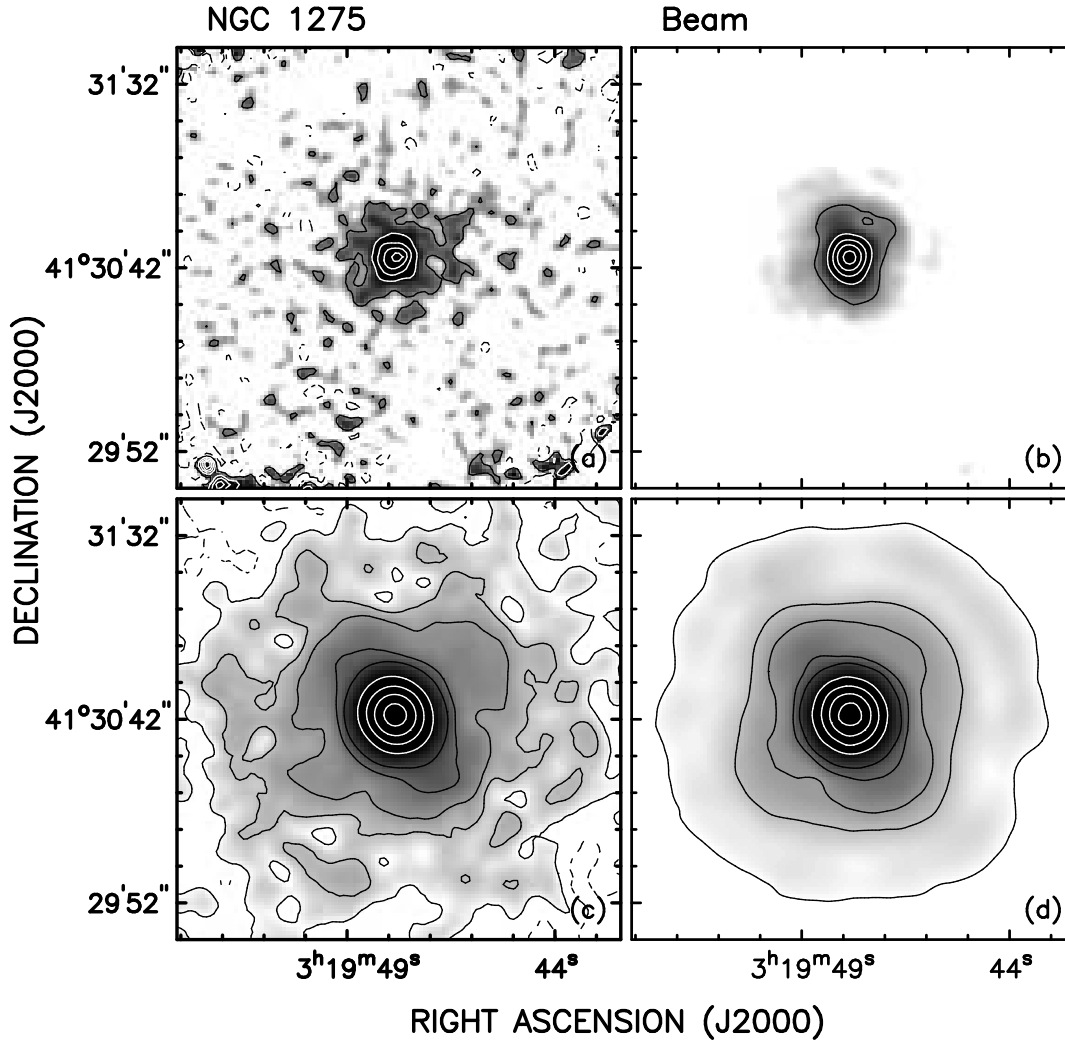


**Figure 1.** Maps of NGC 1275 and the coadded beam maps at  $450\mu\text{m}$  (top row) and  $850\mu\text{m}$  (bottom row). Contours in the  $450\mu\text{m}$  map of NGC 1275 are drawn at  $-10, 10, 30, 50, 70,$  and  $90\%$  of the peak intensity ( $0.78\text{ Jy/beam}$ ). Grayscales start at  $3\%$  level on a logarithmic scale. Contours in the  $850\mu\text{m}$  map are drawn at  $-0.3, 0.3, 1, 2, 5, 10, 30, 50, 70, 90\%$  of the peak intensity ( $1.44\text{ Jy/beam}$ ). Grayscales start at  $0.3\%$  of the peak intensity. The contours and grayscales in the beam maps represent the same percentiles of the peak intensity as in the corresponding maps of NGC 1275.

show both negative and positive contours so that the noise is well illustrated. Since all subtracted clean components are associated with the central bright core, the residual maps represent core-subtracted emission. At  $450\mu\text{m}$ , the core-subtracted map is dominated by noise which is about 10 times higher than that of the  $850\mu\text{m}$  map (see figure caption). At  $850\mu\text{m}$  (Fig. 2f), the noise is much lower, so some additional errors associated with subtracting the central source also show up, the largest of which are within the central  $30''$  region. Since positive residual emission could be real, we take the negative residual emission in this region to represent the errors from the subtraction process. Applying a  $2\sigma$  cutoff to the core-subtracted and total intensity maps, we formed a ratio map to indicate the relative error in this region, finding an average error of  $3.0\%$  and a maximum error of  $6.7\%$ .

Is the resulting emission due to continuum alone?

Bridges & Irwin (1998) have detected  $\text{CO}(J=3-2)$  emission in NGC 1275 at points within  $\pm 7''$  of the core. Their  $\text{CO}(J=3-2)$  beam of  $14''$  is similar to our SCUBA  $850\mu\text{m}$  beam of  $16''$ . The CO line occurs at a redshifted frequency of  $339.9\text{ GHz}$  and is therefore within the  $30\text{ GHz}$ -wide SCUBA band which is centered at  $347\text{ GHz}$ . Bridges & Irwin find an integrated intensity of  $12\text{ K km s}^{-1}$  which corresponds to  $8.6\text{ mJy beam}^{-1}$  when diluted by the  $30\text{ GHz}$  bandwidth (assuming constant response across the band). The value will be smaller when the bandpass response is considered (see Holland et al. 1999). This corresponds to only  $0.6\%$  of the SCUBA flux of  $1.42\text{ Jy}$  within a  $16''$  beam and is well within the noise. Thus, there is no contamination by the CO line at the core and we do not expect any contamination at locations away from the core, either, where no CO emission has been detected.

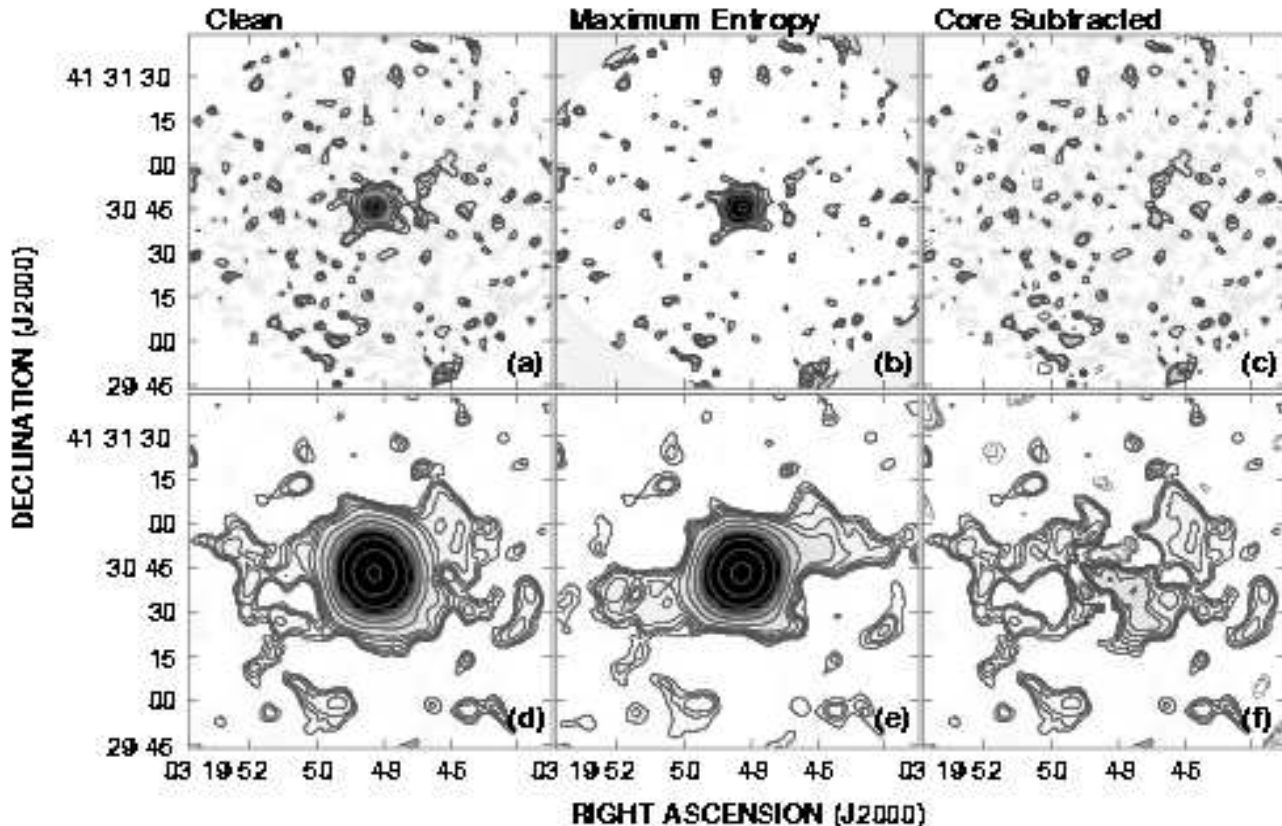


**Figure 2.** Processed (clean, maximum entropy and core-subtracted) maps of NGC 1275. (a) Clean map at  $450\mu\text{m}$ . The image was cleaned to the first negative component and all cleaned components are associated with the strong central source. The greyscale ranges from 0 to  $0.7 \text{ Jy beam}^{-1}$  and contours are at 75 ( $2\sigma$ ), 100, 140, 225, 450, and  $700 \text{ mJy beam}^{-1}$  with a peak at  $756 \text{ mJy beam}^{-1}$ . The clean beam size is  $9.1'' \times 8.8''$  @ position angle  $\text{PA} = 63.3^\circ$ . (b) Maximum entropy map at  $450 \mu\text{m}$ . Contours are at 28, 50, 100, 200, 400, and  $650 \text{ mJy beam}^{-1}$  and the greyscale is from 0 to  $0.35 \text{ Jy beam}^{-1}$ . The beam is the same as in (a). (c) Residual map formed from map (a) but with the strong central source subtracted. The greyscale ranges from 0 to  $0.7 \text{ Jy beam}^{-1}$  and contours are at -100, -75, 75 and  $100 \text{ mJy beam}^{-1}$ . (d) Clean map at  $850\mu\text{m}$  using the same procedure as at  $450\mu\text{m}$ . The greyscale ranges from 0 to  $0.3 \text{ Jy beam}^{-1}$  and the contours are at 7 ( $\approx 2\sigma$ ), 8.5, 10, 13, 18, 25, 50, 100, 200, 400, 800, and  $1350 \text{ mJy beam}^{-1}$ . The peak flux is  $1.44 \text{ Jy beam}^{-1}$ . The clean beam has parameters,  $17.1'' \times 15.7''$  at  $\text{PA}=1.7^\circ$ . (e) Maximum entropy map. The contours are the same as in (d) except for the lowest level which has been set to  $6 \text{ mJy beam}^{-1}$ . The greyscale ranges from 0 to  $0.32 \text{ Jy beam}^{-1}$ . The beam is the same as in (d). (f) Residual map after subtracting the central source. The greyscale ranges from 0 to  $0.3 \text{ Jy beam}^{-1}$  and contours are at -25, -18, -13, -10, -8.5, -7, 7, 8.5, 10, 13, 18, 25, and  $50 \text{ mJy beam}^{-1}$ .

### 3 RESULTS

The processed images (Fig. 2) show that the  $450 \mu\text{m}$  and  $850 \mu\text{m}$  emission is dominated by the bright AGN in NGC 1275. However, fainter extended emission is also observed and appears to be real. Since the core is quite prominent in the processed maps, it has been possible to separate it from the extended emission and results from this process, along with total fluxes and the spectral index, are given in Table 2.

#### 3.1 The AGN

The bright AGN in NGC 1275 has shown a gradual decline of a factor 4 in brightness at 375 GHz ( $800 \mu\text{m}$ ) between 1988 and 1992 (Stevens et al. 1994), providing compelling evidence for the non-thermal nature of this emission. From our data, there is no indication for variability between the three epochs of the present SCUBA observations to the level

of the calibration error, or about 6%. Moreover, our measured 1998 total flux at  $850 \mu\text{m}$  of  $1.6 \text{ Jy}$  agrees closely with the  $800\mu\text{m}$  flux of  $\sim 1.6 \text{ Jy}$  measured by Stevens et al. (from their Fig. 2) in 1994. Thus, the strong decline seen before 1994 does not appear to have continued over the 4 years between 1994 and 1998.

The core is 1.8 times brighter at  $850\mu\text{m}$  than at  $450\mu\text{m}$ , resulting in a spectral index (Table 2) of  $\alpha = -0.88 \pm 0.09$  ( $S_\nu \propto \nu^\alpha$ ). This agrees with the value found by Stevens et al. (1994) of  $\alpha = -0.92 \pm 0.17$  between 375 and 150 GHz over a 6 year monitoring period. Such a steep spectral index can be produced from synchrotron emission. Thus we are likely observing the high frequency extension of the synchrotron emission seen at lower frequencies. It is not possible to extrapolate the low frequency radio flux to the sum-mm because of the variability of the source over the different epochs of observation. However, since the low frequency (i.e.

**Table 2.** NGC 1275 Measured Parameters

Parameter	450 $\mu$ m	850 $\mu$ m
Total Flux (Jy) <sup>a</sup>	1.2 $\pm$ 0.3	1.60 $\pm$ 0.16
Core Flux (Jy) <sup>b</sup>	0.81 $\pm$ 0.03	1.42 $\pm$ 0.03
Core Position <sup>c</sup>		
RA (h, m, s)	03 19 48.26 $\pm$ 0.02	03 19 48.29 $\pm$ 0.03
DEC ( $^{\circ}$ , $'$ , $''$ )	41 30 45.1 $\pm$ 0.3	41 30 43.5 $\pm$ 0.4
Core Size <sup>c</sup>		
Major Axis (arcsec)	4.7 $\pm$ 0.5	— <sup>c</sup>
Minor Axis (arcsec)	3.2 $\pm$ 0.5	— <sup>c</sup>
Position Angle (degrees)	90 $\pm$ 10	— <sup>c</sup>
$\alpha_{Tot}$ <sup>d</sup>	-0.45 $\pm$ 0.28	
$\alpha_{Core}$ <sup>e</sup>	-0.88 $\pm$ 0.09	

<sup>a</sup> The error in the flux reflects the calibration error noted in Sect. 2.1. Errors associated with varying the box size to include or exclude low S/N peaks at larger radii are smaller than this.

<sup>b</sup> The core parameters were derived from gaussian fits to the core component alone, averaging results from fits to the total intensity maps as well as the map of the core alone which was reconstructed from the clean components. The errors include differences between the maps and, in the case of the flux, differences between values measured from integration of the core map, and values determined by the gaussian fit to the core. Note that the calibration error and the pointing error ( $< 1$  arcsecond) are not included in these quoted errors.

<sup>c</sup> A dash means unresolved.

<sup>d</sup>  $S_{\nu} \propto \nu^{\alpha}$

between  $\lambda 90$  cm and  $\lambda 199$  cm) spectral index within the central 1 arcminute region is dominated by a flat spectral index core (see Pedlar et al. 1990), the total synchrotron spectral index must turn over between the low frequency and sub-mm regimes. Given the steepness of the sub-mm spectrum, there is no need to postulate the presence of a dust component in the core at any significant level. A similar conclusion is reached by Leeuw, Samson & Robson (2000) for the elliptical galaxy, NGC 4374, in which sub-mm emission from the AGN core is detected. Note that this does not, by itself, rule out the possibility of some dust in the core. Indeed, the presence of CO emission at the position of the core (Bridges & Irwin 1998, Reuter et al. 1993) suggests that dust is also present there. However, the core is unlikely to be dominated by dust emission or else the core spectral index would be significantly flatter or inverted. The sub-mm core is unresolved at 850 $\mu$ m but has a (deconvolved) size of  $\sim 4''$  at 450 $\mu$ m.

If we use the core spectral index and extrapolate the core flux to 100 $\mu$ m, we find a 100 $\mu$ m core flux of 0.22 Jy. This is within the error bar of the total 100 $\mu$ m flux of  $7.9 \pm 1$  Jy measured by Lester et al. (1995) and suggests that the nonthermal core is a negligible contributor to the total flux at 100 $\mu$ m. Thus, the 100 $\mu$ m total flux (7.9 Jy) can be interpreted as being entirely due to dust emission. This agrees with Lester et al.'s conclusion that less than 20% of the total 100 $\mu$ m emission can be due to the nonthermal core based on the known variability of the core and the constancy of the 100 $\mu$ m flux. Thus, the total emission changes from being non-thermal core-dominated to dust-dominated between 450 $\mu$ m and 100 $\mu$ m.

### 3.2 Extended Emission

The extended sub-mm emission is much fainter than that associated with the core, but is seen at both frequencies and appears to be real. The clean and maximum entropy maps also show good agreement although there are some differences at low contour levels in the 850 $\mu$ m maps. Single epoch maps were also cleaned to confirm that the extended emission is present at all epochs to a level that is consistent with the shorter integration time per epoch and higher atmospheric opacity in the July 15 observations. The extended emission constitutes  $\sim 33\%$  of the total flux at 450 $\mu$ m and  $\sim 11\%$  of the total flux at 850 $\mu$ m.

The 450 $\mu$ m core-subtracted map (Fig. 2c) has a much higher noise level than the 850 $\mu$ m map, but does show several features which remain upon smoothing to lower resolution and which also have counterparts in the 850 $\mu$ m map. The principle one is an elongated feature to the west of the core extending northwards. This will be referred to as the NW extension. Secondly, there are some residual peaks about  $45''$  to the south-east of the core which again have a counterpart in the 850 $\mu$ m map. We will refer to this region as the SE peak. Another peak about  $1'$  to the south-west could possibly be real, but this is not certain given its offset from a nearby 850 $\mu$ m peak.

Extended emission is most readily seen in the lower noise 850 $\mu$ m maps (Fig. 2d, e, and f). These show further extensions to both the east and west and “disconnected” features elsewhere which appear to be real, given their presence in each frame. A fairly strong feature near the core is also seen to extend  $\sim 30''$  to the south-west. This latter feature also appears to be real, though may contain a relatively larger error, given its proximity to the core.

The spectral index of the total emission (Table 2) is flatter than that of the dominant core alone, suggesting that

the spectral index of the faint extended emission may have an inverted (positive) spectral index. Indeed, we could measure this spectral index in two positions, the NW extension and the SE peak, by first smoothing the  $450\mu\text{m}$  map to the  $850\mu\text{m}$  resolution. For the NW extension, flux measurements were made within a  $6''$  diameter region centered at RA =  $03^{\text{h}} 19^{\text{m}} 45^{\text{s}}.79$ , DEC =  $41^{\circ} 30' 57''.3$ , with the resulting spectral index found to be  $\alpha = +2.6$ . For the SE peak, the measurement was made within a  $6''$  diameter region centered at RA =  $03^{\text{h}} 19^{\text{m}} 49^{\text{s}}.17$ , DEC =  $41^{\circ} 30' 00''.3$ , and found to be  $\alpha = +2.8$ . Thus, where the spectral index could be measured, the values are strongly positive. These are clearly dust components.

### 3.2.1 Dust Temperature

Dust is expected to be optically thin at sub-mm wavelengths, and the temperature can, in principle, be determined via  $S_{\nu} = \Omega B_{\nu}(T) Q(\nu)$  (e.g. Stevens & Gear 2000), where  $S_{\nu}$  is the flux density at frequency,  $\nu$ ,  $\Omega$  is the solid angle subtended by the dust,  $B_{\nu}(T)$  is the Planck function applicable to a dust temperature,  $T$ , and  $Q(\nu)$  is the frequency-dependent emissivity of the grains. In the optically thin limit,  $Q(\nu) = (\frac{\nu}{\nu_0})^{\beta}$ , where  $\beta$  is the index of the emissivity law and  $\nu_0$  is the frequency at which the dust becomes optically thin. If we restrict the dust temperature determination for NGC 1275 to regions for which fluxes are available at both frequencies (here, taking the NW extension), and assume that the covering factor is the same at the two frequencies, we can estimate a temperature, adopting a value for the unknown emissivity index,  $\beta$ . Taking  $\beta = 1.3$  as was found for M 82 (Hughes, Gear, & Robson 1994; see also Leeuw et al. 2000), we find a dust temperature of 19 K. For  $\beta = 2$  (e.g. Domingue et al. 1999), we find  $T = 11$  K and if  $\beta = 1$  (Lester et al. 1995),  $T = 29$  K. Thus, for reasonable values of  $\beta$ , the dust temperature is constrained from these observations to be between 10 and 30 K.

While most other flux measurements of NGC 1275 have included the non-thermal core flux, we have noted (Sect. 3.1) that the core is a negligible contributor to the total  $100\mu\text{m}$  flux. Thus, the  $100\mu\text{m}$  point should represent dust emission and can also be used to constrain the dust temperature. If we include the  $100\mu\text{m}$  flux (7.9 Jy, Lester et al. 1995) in this analysis, however, we find that the observed flux ratios cannot be reproduced within error bars using single values of  $\Omega$ ,  $\beta$  and  $T$ . This suggests that (at least) a two component model is required. For  $\beta = 1.3$ , the  $100\mu\text{m}/450\mu\text{m}$  ratio implies a temperature of 38 K in comparison to 19 K found from the  $450\mu\text{m}/850\mu\text{m}$  value. Differences in  $\beta$  or  $\Omega$  are also possible. However, we note that there is some evidence for a two-temperature model from a line ratio analysis of the molecular gas as well (Bridges & Irwin 1998). We suspect that dust that is near the non-thermal core may be warmer.

### 3.2.2 Dust Mass and Gas-to-Dust Ratio

The dust mass is determined via  $M_d = S_{\nu} D^2 / [k_{d\nu} B_{\nu}(T)]$ , where  $D$  is the distance to the galaxy and  $k_{d\nu}$  is the dust mass absorption coefficient. We will determine the dust mass using the  $850\mu\text{m}$  flux. This is because it has typically been found (e.g. Alton et al. 2000) that over 90% of observed

$850\mu\text{m}$  emission arises from cold ( $\lesssim 20$  K) dust, (consistent with our best temperature estimate of 19 K) and this cold component constitutes the bulk of galactic dust. Moreover, the lower noise in the  $850\mu\text{m}$  images makes this a better choice for such a calculation. The value of  $k_{d\nu}$  is rather uncertain and has the same frequency dependence as  $Q(\nu)$ . Again, adopting  $\beta = 1.3$  and extrapolating the mass absorption coefficient from the  $100\mu\text{m}$  value of  $2.5 \text{ m}^2 \text{ kg}^{-1}$  (Stevens & Gear 2000) yields  $k_{d\nu} = 0.15 \text{ m}^2 \text{ kg}^{-1}$ . (This is a factor of 2 higher than the value used by Dunne et al. 2000 for their determination of dust mass functions in the local universe.) Applying a dust temperature of 20 K and using  $S_{\nu} = 0.18$  Jy (after core subtraction, see Table 2), we find a dust mass of  $M_d = 5.9 \times 10^7 M_{\odot}$ . A temperature of 40 K would lower this by a factor of 2.5, using  $\beta = 2$  would increase it by a factor of 4.5, and using the noisier  $450\mu\text{m}$  (rather than  $850\mu\text{m}$ ) data would lower it by a factor of 2.6. Thus our best estimate of the dust mass is  $6 \times 10^7 M_{\odot}$  to within a factor of a few. This is the first estimate of the dust mass in this galaxy from spatially resolved emission measurements which correct for the AGN.

This result can be compared with the much lower dust mass of  $7.5 \times 10^5 M_{\odot}$  (adjusted to our distance) found for NGC 1275 by Goudfrooij et al. (1994) using optical absorption measurements. The absorbing dust is confined to a much smaller patchy region to the north-west of the core (Fig. 3f) and constitutes only 1.3% of the total dust mass as determined from our  $850\mu\text{m}$  measurements. Discrepancies between the absorbing and emitting dust masses have been noted by Goudfrooij & de Jong (1995) who suggested that the differences could be due to additional dust which is distributed more broadly than in front of the stellar light distribution alone. Our dust mass and the extended dust distribution seen at  $850\mu\text{m}$  clearly support this view and indicate that there is much more dust in NGC 1275 seen in emission than previously determined from absorption measurements.

Goudfrooij & de Jong (1995) have determined dust masses for 56 Shapley-Ames elliptical galaxies from IRAS observations, finding dust masses in the range,  $10^4$  to  $5 \times 10^6 M_{\odot}$ . Bregman et al. (1998) have also found IRAS dust masses in the same range for E and S0 galaxies. NGC 1275, therefore, has a higher dust mass, by about an order of magnitude, than the other early-type galaxies studied by these authors. However, it is well known that IRAS observations sample somewhat warmer dust than SCUBA and may thereby overestimate the dust temperature, underestimating the resulting mass (Dunne et al. 2000). Therefore the discrepancy between the high dust mass in NGC 1275 and the lower dust masses in E and S0 galaxies may not be as high as an order of magnitude. Also, these galaxies are typically not in a cooling flow environment. Fewer previous measurements have been made of central cooling flow galaxies. Edge et al. (1999), however, find masses between  $3$  to  $5 \times 10^7 M_{\odot}$  for A1835 and A2390 (adjusting to  $H_0 = 75 \text{ km s}^{-1} \text{ Mpc}^{-1}$ ), in closer agreement with our value for NGC 1275.

Armed with these data, we can compute a global gas/dust ratio. For the molecular gas mass, we use  $1.6 \times 10^{10} M_{\odot}$  (Bridges & Irwin 1998) which uses the Galactic CO to H<sub>2</sub> conversion factor, and for the atomic hydrogen mass, we use the value found for the low velocity system

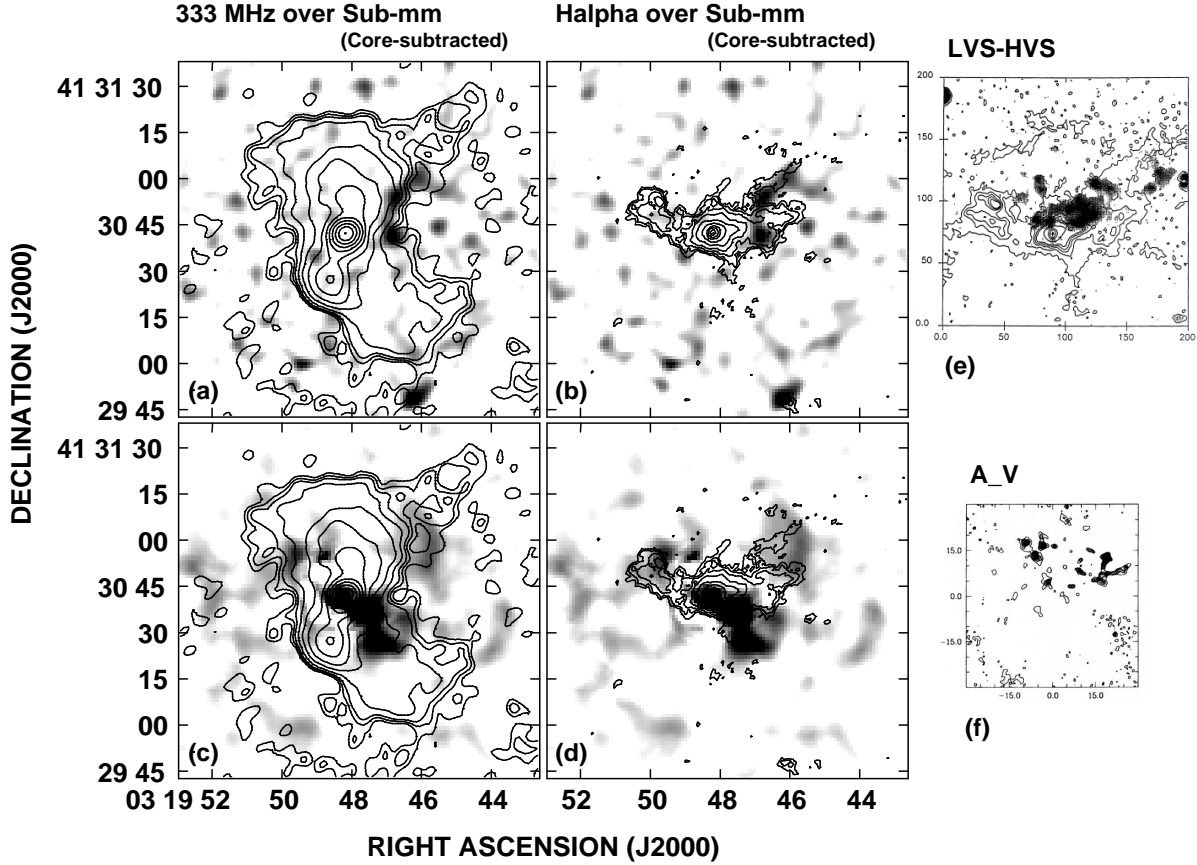


**Figure 3.** Contours of emission at other wavebands over greyscale of the sub-mm emission. (a) 333 MHz radio continuum (Pedlar et al. 1990) over the core-subtracted  $450\mu\text{m}$  emission, the latter smoothed to  $10'' \times 10''$  resolution. The greyscale ranges from 27 to  $90 \text{ mJy beam}^{-1}$  and contours are at 13.5, 20, 28, 50, 100, 200, 400, 800, 1600, 3000, 5000, and  $8000 \text{ mJy beam}^{-1}$ . The 333 MHz beam is  $5''.5 \times 4''.9$  at position angle  $\text{PA} = -74^\circ$ . (b)  $\text{H}\alpha + [\text{NII}]$  emission (Goudfrooij et al. 1994) from the LVS over the same  $450\mu\text{m}$  greyscale as in (a). Contours are in arbitrary units. (c) As in (a) but the  $850\mu\text{m}$  (un-smoothed) core-subtracted emission is the greyscale which scales from 7 to  $25 \text{ mJy beam}^{-1}$ . (d) Contours as in (b) with the greyscale as in (c). (e)  $\text{H}\alpha$  emission showing the low velocity system in contours over the high velocity system in greyscale (Caulet et al. 1992) at the same scale as Figs. (a) through (d). The axes are in units of  $0.406''$ . (f) Optical absorption ( $A_V$ ) from Goudfrooij et al. (1994) at the same scale as Figs. (a) through (e).

by Jaffe (1990), i.e.  $5 \times 10^9 M_\odot$  assuming a spin temperature of 100 K. We find  $M(\text{HI} + \text{H}_2)/M_d \sim 360$  with these assumptions. This is higher than typical Galactic values of 100 to 150 (Devereux & Young 1990) but is consistent with what has been found for radio quiet quasars, spiral galaxies, and ultraluminous infra-red galaxies ( $\approx 260$  to 540; Hughes et al. 1993).

### 3.3 Correlations with other Wavebands

Figure 3 shows overlays of the core-subtracted sub-mm maps (in greyscale,  $450\mu\text{m}$  at top and  $850\mu\text{m}$  at bottom) with emission at other wavebands. Note that by subtracting the core, we cannot compare emission features within the central  $\approx 20''$  diameter region. Overlays are with the 333 MHz radio continuum emission (Fig. 3a, c) which traces the non-thermal component, and with the  $\text{H}\alpha$  low velocity system (Fig. 3b, d) which presumably traces condensing cooling flow gas. For comparison, the high velocity system, associated with the infalling galaxy (Sect. 1), is shown as greyscale

with the LVS contours in Fig. 3e and the optical absorption is shown in Fig. 3f.

The dust emission shows some weak correlations with the 333 MHz map. For example, the sub-mm NW extension occurs along the outer ridge of the radio continuum emission. There is also weak sub-mm emission just where the radio continuum emission falls off about 1 arcminute SW of the nucleus. A ridge of weak radio continuum emission extending from  $\text{RA} = 3^{\text{h}} 19^{\text{m}} 52^{\text{s}}$ ,  $\text{DEC} = 41^\circ 30' 55''$  to  $\text{RA} = 3^{\text{h}} 19^{\text{m}} 49^{\text{s}}$ ,  $\text{DEC} = 41^\circ 29' 50''$  is also seen in the sub-mm.

There is no obvious correlation between the LVS  $\text{H}\alpha$  emission and the sub-mm maps other than a possible one between the NW extension and an  $\text{H}\alpha$  extension at  $450\mu\text{m}$  (Fig. 3b). The HVS  $\text{H}\alpha$  emission (Fig. 3e) occurs in a patchy distribution mainly to the NW of and near the nucleus. Again, there is no clear correlation between the sub-mm emission and high velocity  $\text{H}\alpha$  system other than some correspondence in the same NW extension region. The optical extinction map (see Fig. 3f) does show several knots which correspond to enhanced  $450\mu\text{m}$  or  $850\mu\text{m}$  emission, suggesting that this dust is in the foreground. Nørgaard-Nielsen et al. (1993) and McNamara et al. (1996) have argued that

some of the dust, as observed in optical extinction, corresponds to the intervening (HVS) galaxy.

We have also investigated whether the CO emission (not shown) resembles the sub-mm, since normally dust and molecular gas follow similar distributions. CO has been mapped with similar resolution as the sub-mm by Bridges & Irwin (1998) and Reuter et al. (1993); however, the most wide-scale mapping has been out to a radius of only  $\sim 30''$  and little structure is visible in existing CO maps. Bridges & Irwin do find a bend in the CO contours to the south-west, similar to the bright  $850\mu\text{m}$  emission in that direction. Much higher resolution CO mapping, which cannot be directly compared to our sub-mm distribution due to the core subtraction and difference in resolution, shows an east-west structure similar to the LVS (see Inoue et al. 1996).

Figure 4 shows the  $850\mu\text{m}$  core-subtracted map superimposed on a colour image of the ROSAT HRI X-ray emission which shows a deficit of X-ray flux at the positions of the radio lobes. This morphology has been interpreted as a displacement of the thermal gas by the outflowing radio lobes (Böhringer et al. 1993, Churazov et al. 2000). Fig. 4 shows the best correlation we have found with the sub-mm and helps to explain the partial correlation found between dust and the radio continuum (see above) since there is a relationship between the radio continuum and X-ray emission. The brightest X-ray emission occurs in a ridge which extends from the east of the nucleus and curves to the south. This is also roughly where a weak radio continuum ridge occurs (as pointed out above). The  $850\mu\text{m}$  emission approximately follows this curved ridge (cf. the “filled in” emission in the ME map, Fig. 2e also) although the peaks don’t exactly coincide. For example, dust emission curves around the X-ray peak at RA =  $3^{\text{h}} 19^{\text{m}} 50^{\text{s}}.5$ , DEC =  $41^{\circ} 30' 15''$ . The bright sub-mm extension to the SW of the nucleus truncates abruptly just where the X-ray emission also drops about  $30''$  from the nucleus; this is where the SW radio lobe occurs. To the west of the nucleus, both X-ray and dust emission show an extension to  $\sim 50$  arcseconds, both ending at roughly the same position. The NW extension correlates well with an X-ray peak on the NW side of the galaxy with the sub-mm peak slightly displaced to the NW of the X-ray peak. Even some of the very faint sub-mm emission which we at first considered to be noise bears some resemblance to the X-ray. For example, to the north of the nucleus, the northern X-ray arc has several  $850\mu\text{m}$  peaks occurring along its northern edge about  $45''$  from the nucleus. About 1 arcminute from the nucleus to the NNW, weaker X-ray emission falls off and again, weak peaks of  $850\mu\text{m}$  emission can be seen there.

Recent observations by the Chandra satellite (Fabian et al. 2000) confirm the general characteristics of the X-ray map shown in Figure 4. One improvement is in the clearer view of an X-ray absorption feature  $\sim 40''$  NW of the nucleus which is seen as a small arc just to the west of the brightest X-ray ridge on the NW side of the nucleus (see the low X-ray emission at RA  $\sim 3^{\text{h}} 19^{\text{m}} 45^{\text{s}}$ , DEC  $\sim 41^{\circ} 30' 47''$ ). This absorption feature appears to “wrap around” on the west side of the brightest X-ray/sub-mm peak NW of the nucleus and so suggests that there may be some relation between the dust and the infalling galaxy. However, we do not see enhanced sub-mm emission where the X-ray absorption occurs. This suggests that the feature which is

producing the X-ray absorption includes some component other than dust and/or that the characteristics of the absorbing dust are such that we are not clearly detecting it at  $450\mu\text{m}$  or  $850\mu\text{m}$ .

In summary, we find that the sub-mm dust emission correlates spatially with the X-ray emission, except that there may be offsets between the X-ray peaks and sub-mm peaks (for example, the strongest X-ray peak does not have a counterpart in the sub-mm).

## 4 DISCUSSION

### 4.1 Source of Dust Heating

From these SCUBA data, we have estimated a dust temperature to be  $\sim 20$  K. What are the possible heating sources for this dust? The possibilities include heating by stellar photons, heating by hot electrons in X-ray emitting gas, direct heating by X-rays, and heating by the AGN.

Since dust emission is observed to a distance of  $\sim 1$  arcminute = 20 kpc from the AGN in NGC 1275, we can rule out AGN heating as a possible source for this extended dust. Rigopoulou, Lawrence, & Rowan-Robinson (1996) have also looked at the submillimetre and X-ray data from a number of ultraluminous infra-red galaxies and found that most are well-fitted by a standard model of stellar heating, even when there is evidence for an AGN. Also, since the  $450\mu\text{m}/850\mu\text{m}$  spectral index of the dust emission is the same for dust in the NW extension (measured  $\sim 6$  kpc from the nucleus) as for dust at 15 kpc, there is no need to postulate different heating sources for the extended dust at these frequencies.

Goudfrooij & de Jong (1995) have considered the other heating mechanisms for elliptical galaxies and conclude that direct heating by X-rays is not feasible. This leaves heating by stellar photons and heating by hot electrons as the remaining viable mechanisms. McNamara et al. (1996) have found a faint blue continuum extending out to  $\sim 30$  kpc (1.5 arcminutes) in NGC 1275 along the filamentary H $\alpha$  system, indicating that stars do indeed exist to large distances. However, the close resemblance of the sub-mm continuum in NGC 1275 to the X-ray structure and the apparent absence of a large population of stars more massive than  $\sim 5 M_{\odot}$  (Sarazin & O’Connell 1983, Smith et al. 1992, McNamara et al. 1996) points to hot electrons as the source of dust heating in NGC 1275. Lester et al. (1995) have also shown quantitatively, that hot electrons in NGC 1275 are energetically capable of supplying the dust heating in this galaxy. The fact that the  $850\mu\text{m}$  emission avoids the brightest X-ray peak suggests that dust may be more rapidly destroyed in this region.

### 4.2 Origin of the Dust

These observations have shown that extended dust exists in NGC 1275 to very large distances from the core ( $\sim 20$  kpc) and that the total dust mass is high, i.e.  $6 \times 10^7 M_{\odot}$ , two orders of magnitude larger than that inferred from optical absorption studies. As indicated in Sect. 1, three possibilities for the origin of the dust present themselves: from the cooling flow or in dense clouds associated with the flow, from

ongoing star formation, or from the merger of a gas/dust rich galaxy. Let us consider these possibilities.

If dust is mixed with the cooling flow gas, then its lifetime against destruction by sputtering is found from  $t_d = 2 \times 10^4 \text{ (cm}^{-3}/n)(a/0.01\mu\text{m})$ , where  $n$  is the density of the hot cooling flow gas and  $a$  is the grain radius (Draine & Salpeter 1979). The grain size is uncertain, but a reasonable upper limit is 0.1 micron (cf. Lester et al. 1995), and the hot gas density near the center of NGC 1275 is 0.05 - 0.1  $\text{cm}^{-3}$  (e.g. Fabian et al. 2000). This gives  $t_d = 2 - 4 \times 10^6$  years. Thus, dust will be destroyed on short timescales if it is mixed with the hot gas and there must be a source of dust replenishment. The alternative is that dust is somehow shielded from the X-ray environment, possibly in dense molecular clouds for which there is (as yet) no observational evidence.

If stellar mass loss is continuously replenishing the dust, we would expect this dust to be ejected and dispersed into the X-ray emitting environment, suggesting that the short lifetime determined above should be relevant. Determining a dust mass loss rate from stars is not straightforward and involves a knowledge of the initial mass function, the mass loss rates from stars, and the gas/dust ratio in the ejected material. For NGC 1275, there currently appear to be no stars more massive than  $5 M_\odot$  and, if more massive stars have been produced in the past, this past massive star formation must have ceased 70 Myr ago or more (Smith et al. 1992). Since this is longer than the lifetime of dust in the X-ray emitting environment, we do not expect young, massive O type stars to contribute to the currently observed dust in NGC 1275. The next strongest source of mass loss, and that which will dominate in NGC 1275, comes from the older, more evolved stellar population. The remaining main sequence stars of  $5 M_\odot$  or less contribute negligibly to global mass loss rates (see Snow 1982).

Both Faber & Gallagher (1976) and Knapp, Gunn & Wynn-Williams (1992) have estimated, through independent means, mass-loss rates for an evolved population of stars. Knapp et al. find  $\dot{M} = 2.1 \times 10^{-12} (L_{2.2\mu\text{m}}/L_\odot) M_\odot \text{ yr}^{-1}$  and Faber & Gallagher find  $\dot{M} = 1.5 \times 10^{-11} (L_B/L_\odot) M_\odot \text{ yr}^{-1}$ , where  $L_{2.2\mu\text{m}}$  and  $L_B$  are, respectively, the  $2.2\mu\text{m}$  and blue luminosities. Using (from the NASA Extragalactic Database) the total corrected blue magnitude of 12.15, we find  $\dot{M} = 0.81 M_\odot \text{ yr}^{-1}$  and using the  $2.2\mu\text{m}$  flux density of 159 mJy, we find  $\dot{M} = 0.62 M_\odot \text{ yr}^{-1}$ . The former value should be an overestimate since it includes any contribution from the AGN and the latter should be an underestimate since the  $2.2\mu\text{m}$  flux density is measured only within a central  $32''$  aperture. Taking a mass loss rate of  $0.7 M_\odot \text{ yr}^{-1}$ , then, over  $2 - 4 \times 10^6$  years, stars can contribute, at most,  $2.8 \times 10^6 M_\odot$  of gas to the ISM in NGC 1275. With a gas/dust ratio of 360 (Sect. 3.2.2), the dust mass generated by stars would be  $8 \times 10^3 M_\odot$ , which is 4 orders of magnitude lower than observed. It is possible that 2 orders of magnitude could be gained by allowing dust to survive over a timescale one order of magnitude longer, since then there could be a contribution from hot massive stars which typically have higher mass loss rates than the older stars. However, it is unlikely that 4 orders of magnitude could be gained and a dust shielding mechanism would then also be required. Thus, we conclude that dust cannot be replenished by stellar mass loss. Lester et al. (1995) came to the same conclusion for NGC 1275 and

Goudfrooij & de Jong (1995) have also found that most elliptical galaxies in which X-ray emission has been detected contain more dust than can be accounted for by stellar mass loss. Moreover, if the observed dust originated from stellar mass loss, we would expect the dust distribution to bear some resemblance to the stellar light distribution, which is not observed.

An obvious source of dust is the infalling galaxy. Goudfrooij et al. (1994), in fact, make a case for *all* dust in elliptical galaxies being supplied by external systems, and others (e.g. Pinkney et al. 1996, Koekemoer et al. 1999) have also supported the merger/accretion origin for dust in ellipticals. McNamara et al. (1996) and Nørgaard-Nielsen et al. (1993) have suggested, for NGC 1275, that two dust systems may be present, one associated with NGC 1275 and one associated with the the high velocity system. Martel et al. (1999) also find dust absorption at the north-west location of the HVS. These results find some support from our observations since the HVS is observed to the NW of the core of NGC 1275, as is the NW sub-mm extension. Thus, the infalling galaxy appears to contain dust and, one could argue, is a source of dust.

Several lines of argument support this view. There is accumulating evidence that the infalling galaxy is currently interacting with NGC 1275 (Hu et al. 1983; Unger et al. 1990; Caulet et al. 1992; Nørgaard-Nielsen et al. 1993; Ferruit et al. 1998). The HVS gas occurs in a patchy distribution over  $\sim 20$  kpc, in projection (Fig. 3e), arguing for a broad interaction region (though the region containing dust is larger still by about a factor of 2). The interaction timescale (impulsive approximation) is roughly  $t_i \sim d/v$ , where  $d$  is the size of the target galaxy and  $v$  is the relative velocity of the perturber. If we take the size to be the entire projected region over which dust emission is detected ( $\sim 38$  kpc) and  $v = 3000 \text{ km s}^{-1}$ , we find  $t_i \sim 1 \times 10^7$  yrs. This is a factor of at least 2 higher than the dust destruction timescale, but this may not be largely discordant, given the approximation made. Finally, our dust mass ( $6 \times 10^7 M_\odot$ ) and gas-to-dust ratio (360) are quite typical of spiral and IRAS galaxies, and our dust temperature (20 K) is also typical of spiral galaxies though somewhat cooler than that observed in IRAS galaxies (Alton et al. 2000, Dunne et al. 2000), arguing for an infalling spiral galaxy as the origin of the dust. In this scenario, the dust distribution would resemble the X-ray gas distribution (Fig. 4) because the dust is widely distributed and is being collisionally heated as discussed in Sect. 4.1. The implication is that there should be additional cold dust, as yet undetected, which is widely distributed in NGC 1275. A difficulty with this scenario is that externally supplied dust, initially moving at  $3000 \text{ km s}^{-1}$  with respect to NGC 1275, must “settle” into the rest frame of NGC 1275 while the hot stars and associated  $\text{H}\alpha$  emitting gas do not. A theoretical development involving an infalling spiral galaxy which also interacts with cooling flow gas should be brought to bear on this question.

A final interesting idea is that the dust forms directly in the cooling flow (Fabian et al. 1994, Hansen et al. 1995), which would explain the observed spatial correlation directly. Fabian et al. suggest that dust could form within clouds, even in the absence of dust in the cooling flow originally, and would be shielded against destruction, giving it a longer lifetime than the above-determined value. The tem-

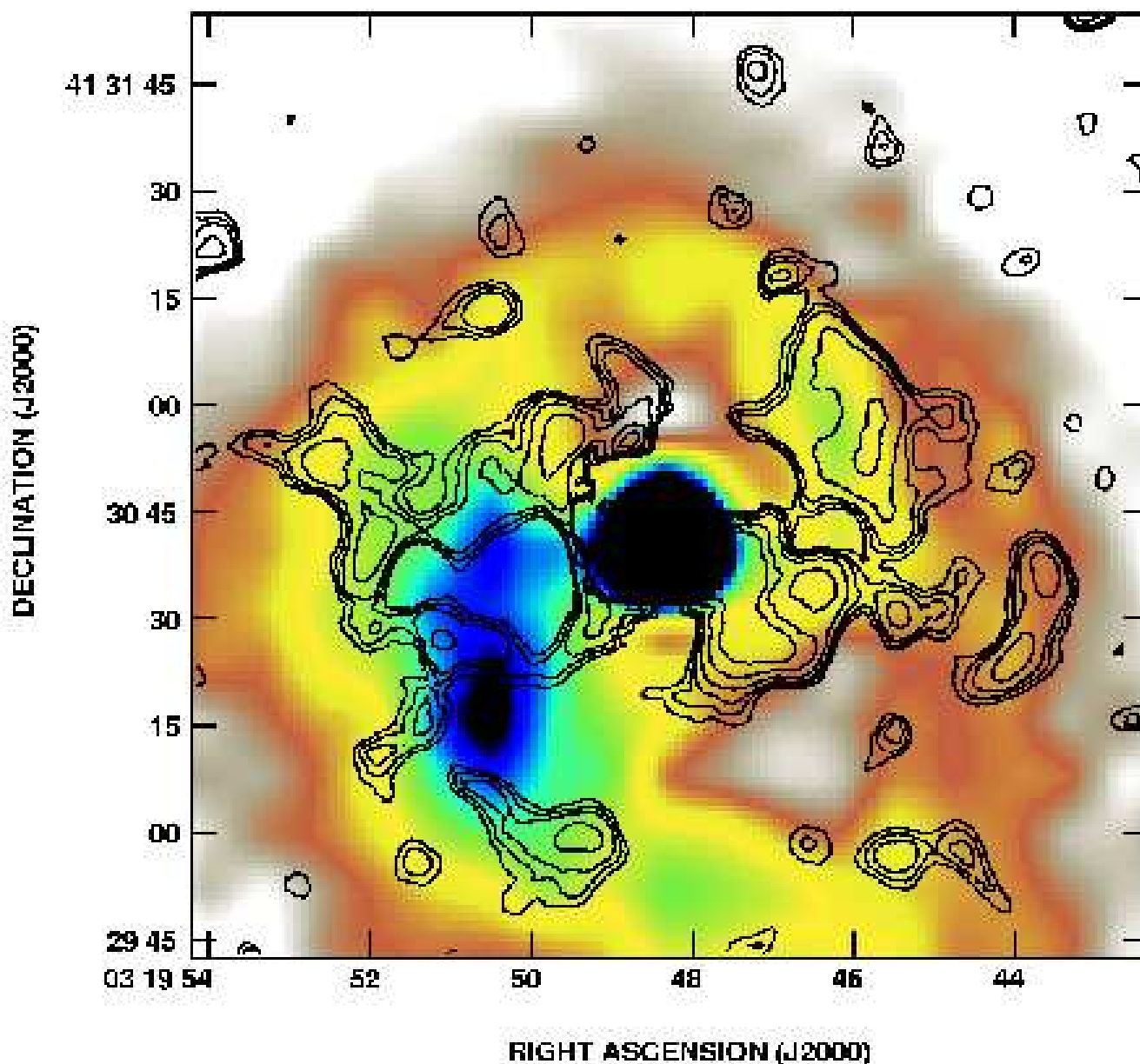


**Figure 4.** Core-subtracted  $850\mu\text{m}$  contours (as in Fig. 2f) over a colour image of the X-ray emission taken from the ROSAT HRI archive (observer, W. Voges, 1994). The colours range (lowest to highest intensity) from grey through red, yellow, green, blue, violet, and black. The low intensity “holes” north and south-west of the nucleus are filled with radio continuum emission (see Fig. 3c); for a similar X-ray image, see Böhringer et al. (1993).

perature of the dust grains is expected to be is very low, with most of the dust at less than 6 K and some as high as 11 K. However, as the clouds become disturbed in the inner part of the cooling flow, external heating should make the dust more visible (and destroy the dust on short timescales again). Since the LVS is known to be associated with the cooling flow as well, however, we would also expect the dust (unless it is rapidly destroyed) to correlate with the LVS in this scenario, for which there is no strong evidence. Thus, this model seems less attractive, although should not be ruled out pending further work on disentangling density from temperature effects in the cooling flow region.

## 5 CONCLUSIONS

We have made SCUBA observations of the cD galaxy, NGC 1275, which is at the center of the Perseus Cluster cooling flow. Emission has been detected at both  $850\mu\text{m}$  and  $450\mu\text{m}$  and, applying standard radio astronomical techniques such as CLEAN and Maximum Entropy to these sub-mm maps, we have removed structures related to the beam shape in order to reveal real low level emission. The resulting sub-mm distribution can be easily separated into a bright central core and fainter extended emission, allowing us to determine the spectral indices of the core and extended emission separately.

The core has a steep spectral index (-0.88) suggest-

ing that it can be explained primarily in terms of a high-frequency extension of the non-thermal AGN emission. The extended emission has a positive spectral index (+2.7), and is clearly due to dust which extends as far as 20 kpc from the nucleus. We estimate the dust temperature to be 20 K (though 10 K to 30 K is possible, depending on the assumed value of the dust emissivity index) and rule out the AGN as the main heating source, given the presence of dust far from the nucleus. The dust mass is  $6 \times 10^7 M_{\odot}$  (within a factor of a few); this dust mass is higher by 2 orders of magnitude than that inferred from optical extinction. Thus there is much more dust in this galaxy than previously realized. The gas-to-dust ratio is found to be 360. Note that the latter value is derived using an assumption of a Galactic CO to H<sub>2</sub> conversion factor as well as a 100 K spin temperature for neutral hydrogen. Nevertheless, the derived dust mass, gas-to-dust ratio, and dust temperature are all typical of values being found for spiral galaxies.

A remarkable correlation between the sub-mm dust emission and the X-ray emission is observed in this galaxy, although there are some displacements in emission peaks. When the various sources of dust heating are considered, the strongest case can be made for collisional heating by hot X-ray emitting electrons. This would explain the spatial correlation between the two components. Since the grain destruction timescale is short ( $\sim 4 \times 10^6$  yrs), continuous dust replenishment is required to account for the sub-mm emission. We have ruled out stars as the source of dust and suggest instead that the infalling galaxy is the most likely candidate, given that the observed dust parameters are typical for spiral galaxies. Thus, we have a picture in which the infalling galaxy is interacting with NGC 1275 over a large region, supplying it with dust which is then heated most effectively by collisions with hot electrons in the cooling flow gas. If this scenario is correct, then more cold dust should be present in NGC 1275 than we have detected. The alternative is that dust forms directly in the cooling flow and is shielded from destruction. Further spatially resolved multi-wavelength observations should be able to distinguish between these scenarios by disentangling density from temperature effects.

## ACKNOWLEDGMENTS

This research has made use of data obtained through the High Energy Astrophysics Science Archive Research Center Online Service, provided by the NASA/Goddard Space Flight Center. We are grateful to A. Pedlar and P. Goudfrooij for providing FITS images of their published data and also to Dr. A. Caulet for her assistance.

## REFERENCES

Allen S.W., 2000, MNRAS, 315, 269  
 Allen S. W., Fabian A. C., 1997, MNRAS, 286, 583  
 Allen S.W., Fabian A.C., Johnstone R.M., Arnaud K.A., Nulsen P.E.J., 1999, *astroph/9910188*  
 Alton P. B., Xilouris E. M., Bianchi S., Davies J., Kylafis N. 2000, A&A, 356, 795  
 Annis J., Jewitt D., 1993, MNRAS, 264, 593  
 Arnaud K.A., Mushotzsky R.F. 1998, ApJ, 501, 119

Böhringer H., Voges W., Fabian A. C., Edge A. C., Neumann D. M., 1993, MNRAS, 264, L25  
 Bregman J. N., Snider B. A., Grego L., Cox C. V. 1998, ApJ, 499, 670  
 Bridges T. J., Irwin J. A., 1998, MNRAS, 300, 967  
 Briggs S.A., Sniijders M.A.J., Bokserberg A., 1982, Nature, 300, 336  
 Carlson M. N. et al. 1998, AJ, 115, 1778  
 Caulet A., Woodgate B.E., Brown L.W., Gull T.R., Hintzen P., Lowenthal J.D., Oliverson R.J., Ziegler M.M., 1992, ApJ, 388, 301  
 Churazov E., Forman W., Jones C., Böhringer H., 2000, A&A, 356, 788  
 Clark B. G., 1980, A&A, 89, 377  
 Cornwell T. J., Evans K. F., 1985, A&A, 143, 77  
 Cox C.V., Bregman J.N., Schombert J.M., 1995, ApJS, 99, 405  
 Crawford C.S., Allen S.W., Ebeling H., Edge A.C., Fabian A.C., 1999, MNRAS, 306, 857  
 Devereux N. A., Young J. S., 1990, ApJ, 359, 42  
 De Young D.S., Roberts M.S., Saslaw W.C. 1973, ApJ, 185, 809  
 Domingue D. L., Keel W. C., Ryder S. D., White III R. E., 1999, AJ, 118, 1542  
 Donahue M., Mack J., Voit G.M., Sparks W., Elston R., Maloney P.R., 2000, *astroph/0007062*  
 Draine B.T., Salpeter E., 1979, ApJ, 231, 77  
 Dunne L., Eales S., Edmunds M., Ivison R., Alexander P., Clements D. L., 2000, MNRAS, 315, 115  
 Edge A.C., Ivison R.J., Smail I., Blain A.W., Kneib J.-P., 1999, MNRAS, 306, 599  
 Faber S. M., Gallagher J. S. 1976, ApJ, 204, 365  
 Fabian A.C., 1994, ARA&A, 32, 227  
 Fabian A.C., Johnstone R.M., Daines S.J., 1994, MNRAS, 271, 737  
 Fabian A.C., Hu E.M., Cowie L.L., Grindlay J. 1981, ApJ, 248, 47  
 Fabian A.C., Sanders J.S., Ettori S., Taylor G.B., Allen S.W., Crawford C.S., Iwasawa K., Johnstone R.M., Ogle P.M., 2000, MNRAS, 318, 65  
 Ferruit P., Adam G., Binette L., Pecontal E., 1998, NewA, 2, 345  
 Gear W.K., Robson E.I., Gee G., Nolt I.G., 1985, MNRAS, 217, 281  
 Goudfrooij P., de Jong T., 1995, A&A, 298, 784  
 Goudfrooij P., Hansen L., Jørgensen H. E., Nørgaard-Nielsen H. U., 1994, A&AS, 105, 341  
 Hansen L., Jørgensen H. E., Nørgaard-Nielsen H. U. 1995, A&A, 297, 13  
 Hansen L., Jørgensen H.E., Nørgaard-Nielsen H.U., Pedersen K., Goudfrooij P., Linden-Vornle M.J.D., 2000, A&A, 362, 133  
 Holland W. S., et al. 1999, MNRAS, 303, 659  
 Hu E.M., 1992, ApJ, 391, 608  
 Hu E.M., Cowie L.L., Kaaret P., Jenkins E.B., York D.G., Roesler F.L., 1983, ApJ, 275, 27  
 Hughes D. H., Gear W. K., Robson E. I., 1994, MNRAS, 270, 641  
 Hughes D. H., Robson E. I., Dunlop J. S., Gear W. K., 1993, MNRAS, 263, 607  
 Inoue, M. Y., Kamenno, S., Kawabe, R., Inoue, M., Hasegawa, T., & Tanaka, M. 1996, AJ, 111, 1852  
 Jaffe W. 1990, A&A, 240, 254  
 Jaffe W., Bremer M.N., van der Werf P.P., 2000, *astroph/0009418*  
 Johnstone R.M., Fabian A.C., Taylor G.B. 1998, MNRAS, 298, 854  
 Koekemoer A.M., O'Dea C.P., Sarazin C.L., McNamara B.R., Donahue M., Voit G.M., Baum S.A., Gallimore J.F. 1999, ApJ, 525, 621  
 Knapp G. R., Gunn J. E., Wynn-Williams C. G. 1992, ApJ, 399, 76  
 Krabbe A., Sams III B.J., Genzel R., Thatte N., Prada F., 2000, A&A, 354, 439

- Leeuw L. L., Sansom A. E., Robson E. I., 2000, MNRAS, 311, 683
- Lester D.F., Zink E.C., Doppmann G.W., Gaffney N.I., Harvey P.M., Smith B.J., 1995, ApJ, 439, 185
- Lynds R. 1970, ApJ, 159, 151
- Martel A. R., et al., 1999, ApJS, 122, 81
- McNamara B. R., O'Connell R. W., Sarazin C. L. 1996, AJ, 112, 91
- Minkowski R. 1957, in *Proceedings from 4th IAU Symposium*, edited by H.C. Van de Hulst, CUP, pg. 107
- Nørgaard-Nielsen H. U., Goudfrooij P., Jørgensen H. E., Hansen L. 1993, A&A, 279, 61
- O'Dea C.P., Baum S.A., Gallimore J.F. 1994, ApJ, 436, 669
- Pedlar A., Ghataure H.S., Davies R.D., Harrison B.A., Perley R., Crane P.C., Unger S.W., 1990, MNRAS, 246, 477
- Pinkney J., et al., 1996, ApJ, 468, L13
- Reuter H.-P., Pohl M., Lesch H., Sievers A. W. 1993, A&A, 277, 21
- Sandell G. 1997, "The SCUBA mapping cookbook, A first step to proper map reduction", available at <http://www.jach.hawaii.edu/JACpublic/stardocs/sc11.htx/sc11.html>
- Sarazin C. L., O'Connell R. W. 1983, ApJ, 268, 552
- Seyfert C.K. 1943, ApJ, 97, 28
- Smith E. P. et al. 1992, ApJ, 396, L49
- Snow T. P. Jr. 1982, ApJ, 253, L39
- Stevens J. A., Gear W. K. 2000, MNRAS, 312, L5
- Stevens J. A., Litchfield S. J., Robson E. I., Hughes D. H., Gear W. K., Terasranta H., Valtaoja E., Tornikoski M., 1994, ApJ, 340, 150
- Unger S.W., Taylor K., Pedlar A., Ghataure H.S., Penston M.V., Robinson A. 1990, MNRAS, 242, 33
- Voit M., Donahue M. 1995, ApJ, 452, 164
- White D.A., Fabian A.C., Johnstone R.M., Mushotzsky R.F., Arnaud K.A. 1991, MNRAS, 252, 72

This paper has been produced using the Royal Astronomical Society/Blackwell Science L<sup>A</sup>T<sub>E</sub>X style file.